The Astrophysical Journal, 963:67 (15pp), 2024 March 1 https://doi.org/10.3847/1538-4357/ad1f6d

Predicting Cloud Conditions in Substellar Mass Objects Using Ultracool Dwarf Companions

Emily Calamari[1,2], Jacqueline K. Faherty[2], Channon Visscher[3,4], Marina E. Gemma[5,6], Ben Burningham[7], and Austin Rothermich[1,2]
[1] The Graduate Center, City University of New York, New York, NY 10016, USA
[2] Department of Astrophysics, American Museum of Natural History, New York, NY 10024, USA
[3] Department of Chemistry and Planetary Sciences, Dordt University, Sioux Center, IA, USA
[4] Center for Exoplanetary Systems, Space Science Institute, Boulder, CO, USA
[5] Department of Geosciences, Stony Brook University, Stony Brook, NY 11794, USA
[6] Department of Earth and Planetary Sciences, American Museum of Natural History, New York, NY 10024, USA
[7] Centre for Astrophysics Research, Department of Physics, Astronomy and Mathematics, University of Hertfordshire, Hatfield AL10 9AB, UK
Received 2023 November 6; revised 2024 January 6; accepted 2024 January 7; published 2024 February 29

Abstract

We present results from conducting a theoretical chemical analysis of a sample of benchmark companion brown dwarfs whose primary star is of type F, G, or K. We summarize the entire known sample of these types of companion systems, termed "compositional benchmarks," that are present in the literature or recently published as key systems of study in order to best understand brown dwarf chemistry and condensate formation. Via mass balance and stoichiometric calculations, we predict a median brown dwarf atmospheric oxygen sink of $17.8^{+1.7}_{-2.3}\%$ by utilizing published stellar abundances in the local solar neighborhood. Additionally, we predict a silicate condensation sequence such that atmospheres with bulk Mg/Si $\lesssim$0.9 will form enstatite ($MgSiO_3$) and quartz (SiO_2) clouds, and atmospheres with bulk Mg/Si $\gtrsim$0.9 will form enstatite and forsterite (Mg_2SiO_4) clouds. The implications of these results on C/O ratio trends in substellar-mass objects and the utility of these predictions in future modeling work are discussed.

Unified Astronomy Thesaurus concepts: Brown dwarfs (185); Main sequence stars (1000); Wide binary stars (1801); Exoplanet atmospheres (487); Atmospheric clouds (2180); Astrochemistry (75)

1. Introduction

Since the first brown dwarf was confirmed in 1995 (Nakajima et al. 1995; Rebolo et al. 1995), astronomers have worked to establish a set of spectral standards (Kirkpatrick 2005), i.e., objects whose features define a given spectral type, as well as characteristic standards (e.g., Pinfield et al. 2006; Faherty et al. 2010; Gagné et al. 2015), i.e., objects for which properties like age and/or metallicity are independently known. These standards outline and define the changing temperature structures and chemical processes that occur in ultracool dwarf (UCD) atmospheres. Defining this sequence of standards is essential in order to calibrate and test cutting-edge evolutionary, photometric and spectral models (e.g., Burningham et al. 2009, 2013). While our understanding of brown dwarf science has advanced significantly in the near 30 yr since the first spectral standards were discovered, countless open questions remain about the physical and chemical nature of these objects. To name a few: what types of convective processes and/or thermochemistry drives differences between observed and model spectra? What causes the appearance of observable atmospheric clouds and/or variability in certain objects? How can we determine the formation history of an object from observational data? While this work does not attempt to put forth definitive answers to these questions, we do propose a path forward for those who seek to do so through careful examination of brown dwarf characteristic standards, known as "benchmarks."

Individual characterization of brown dwarf atmospheres and fundamental parameters (age, mass, effective temperature ($T_{\rm eff}$), and radius) is impeded by the age–mass–temperature degeneracy that exists due to the thermal evolution of these objects. Benchmark brown dwarfs provide the potential to break this degeneracy with the use of independently known parameters. One particularly useful subset of benchmarks consists of co-movers and companions—those that (a) belong to a moving group or cluster where the bulk properties of the collection of stars (e.g., age, metallicity, and dynamic history) can be inferred (e.g., Bowler et al. 2015; Gagné et al. 2015; Faherty et al. 2016) or (b) are co-moving in binary or multiple-star systems where a detailed study of the primary companion star(s) can provide information for each object in the system (e.g., Pinfield et al. 2006; Faherty et al. 2010; Crepp et al. 2012; Deacon et al. 2014). Our focus in this work is on benchmark brown dwarfs belonging to a binary or multiple system with the specification that the primary star in the system is of spectral type F, G, or K. In doing so, we aim to map the chemistry of nearby UCDs to the solar neighborhood population ($\leqslant$100 pc).

Chemical mapping is one route in exploring the possible origins and evolutionary pathways of stars and planets within our galaxy. This approach has been taken by galactic cartographers to understand large-scale chemical structure of disk stars (e.g., Twarog 1980; Hawkins 2023) as well as by solar neighborhood cartographers focusing on exoplanet host star abundances (e.g., Adibekyan et al. 2012; Teske et al. 2019; Delgado Mena et al. 2021). The chemical characterization of local solar-type (FGK) stars has several benefits: these data are

grounded against the precise chemical abundances of our Sun (i.e., Lodders 2021), these spectra are free from molecular absorption bands that make M-type dwarfs difficult to characterize (see Tsuji & Nakajima 2014; Tsuji et al. 2015), and meteoritic data have established a near 1:1 relationship between solar abundances and primitive condensed material in the protoplanetary disk (Lodders 2003, 2021).

To ground what types of chemistry we might expect in UCD atmospheres, Brewer & Fischer (2016) found that local ($\sim<$ 350 pc) FGK stars have a carbon-to-oxygen (C/O) ratio distribution peaked around 0.47 (lower than that reported for the Sun at 0.55 by Lodders (2021)) with a steep drop-off at supersolar values such that no stars in their sample had a C/O $>$ 0.7. This leaves the potential for carbon-rich atmospheres in the solar neighborhood (C/O $>$ 0.65) to be $<$ 0.13%. Additionally, Brewer & Fischer (2016) found that the magnesium-to-silicon (Mg/Si) ratio peaks around 1.0, with a broad distribution ranging from 0.8 to 1.4, where roughly 60% of systems have 1 $<$ Mg/Si $<$ 2. To understand the population of nearby brown dwarfs, it is extremely useful to place them in context with what we currently know about the chemical distribution of the solar neighborhood, and how this agreement or disagreement can inform UCD atmospheric chemistry and formation pathways.

With the use of the spectral inversion, or "retrieval," modeling technique (Line et al. 2015; Burningham et al. 2017), we have been able to probe the atmospheres of brown dwarfs and approximate molecular abundances from spectral data. However, even with these methods, converting from atmospheric molecular to bulk atomic abundance is a nontrivial task, as we know metal condensates ($MgSiO_3$, Mg_2SiO_4, Al_2O_3, etc.) will sequester atoms into clouds starting from the high photosphere down into the deep, unobservable interior. A major participant of this thermochemical process is oxygen, due to its relatively high abundance in these atmospheres and its ability to form both volatile species (e.g., CO, CH_4, H_2O, etc.) and refractory condensates (e.g., Mg_2SiO_4, $MgSiO_3$, Al_2O_3, etc.). As a result, retrieving a reliable oxygen abundance for UCD atmospheres has been challenging (see, e.g., Line et al. 2017; Calamari et al. 2022; Zalesky et al. 2022). To date, the attempts to account for oxygen sequestered in unobservable condensates have relied on an approximate correction factor from solar-ratio, thermochemical calculations done in Burrows & Sharp (1999) (in which the dominating oxygen sink for atmospheres $<$ 2200 K is enstatite ($MgSiO_3$) clouds), or the estimated removal of $\sim$20%–23% of bulk oxygen based upon the abundances of rock-forming elements in a solar-composition gas (Visscher & Fegley 2005; Visscher et al. 2010b). The inability to accurately measure oxygen abundances directly impacts all of the aforementioned open questions in brown dwarf science. This inhibits not only understanding of the thermochemical and dynamical processes that govern these atmospheres, but also measurements of fundamental properties like metallicity and C/O ratio that may reveal formation history.

To focus on answering some of these open questions, we revisit the work of earlier chemical models (Allard et al. 1997; Burrows & Sharp 1999; Ackerman & Marley 2001; Marley et al. 2002; Visscher & Fegley 2005; Visscher et al. 2010a, 2010b) and update these assumptions to include an oxygen sink correction that is reflective of non-solar abundances and considers other minor refractory condensates that could shape observable spectra. By focusing on brown dwarf systems co-moving with a solar-type star and utilizing the bulk chemistry known for the primaries in these benchmark systems, we estimate condensate species and abundance based on a given system's unique stellar, rather than solar, bulk abundances. For this theoretical framework, we will employ mass-balance constraints and stoichiometric procedures found in previous thermochemical equilibrium studies of condensate formation in UCD atmospheres (Lodders 2002; Visscher & Fegley 2005; Visscher et al. 2010a; Wakeford et al. 2017). By using a more accurate assessment of the chemical context of stellar systems, we aim to provide a more rigorous guide to estimating the loss of oxygen to clouds in UCD atmospheres by taking advantage of the full data set on benchmark brown dwarfs.

In Section 2, we discuss the utility of benchmark brown dwarfs in addressing current open questions in brown dwarf science, and we present the updated summary of companion benchmark systems (Section 2.1). In Section 3, we discuss the importance of L-type dwarf benchmarks in constraining atmospheric chemistry as it relates to cloud model solutions and their impact on UCD modeling as a whole. In Section 4, we outline the chosen published stellar abundance data set and the subsequent subset of companion benchmarks highlighted. In Section 5, we give an overview of the theoretical gaseous absorbers and condensate species we expect to find in UCD atmospheres. In Section 6, we outline the theoretical thermochemical framework and assumptions used in order to carry out this work. In Section 7, we present our results from applying thermochemical equilibrium calculations to a collection of abundances of solar neighborhood FGK-type stars in order to quantify major oxygen sinks in companion UCD atmospheres. In Section 8, we discuss the implications of these findings on future UCD atmospheric modeling.

2. Significance of Benchmark Brown Dwarfs

The first confirmed methane-bearing brown dwarf was Gliese 229B, which was found co-moving with the nearby M dwarf Gliese 229A. The kinematics and general chemical makeup of Gliese 229A were known at the time; therefore, Gliese 229B was marked a "benchmark" brown dwarf, given that the properties of the primary could be applied to the secondary. The term benchmark is now used more generally to highlight a UCD for which we have external empirical constraints that do not rely on model predictions (e.g., Pinfield et al. 2006; Burningham et al. 2009). By 2010, approximately 70 benchmarks had been discovered and cataloged in the literature (e.g., Burgasser et al. 2005b; Bihain et al. 2010; Faherty et al. 2010; Seifahrt et al. 2010)—a number that has more than doubled in recent years, thanks to large or all-sky surveys such as the Two-Micron All-Sky Survey (2MASS; Skrutskie et al. 2006), Wide-Field Infrared Survey Explorer (WISE; Wright et al. 2010), and Panoramic Survey Telescope and Rapid Response System (Pan-STARRS; Chambers et al. 2016), as well as citizen science projects like the Backyard Worlds Planet 9 Collaboration (see Kuchner et al. 2017; Faherty et al. 2021; Schneider et al. 2021; Rothermich et al. 2023). This subset of brown dwarfs has systematic or spectral information that can lead to a more precise age estimation, metallicity, and/or mass—all of which are extremely difficult parameters to probe independently for UCDs.

The largest (and fastest-growing) sample of benchmark objects comes from those that are widely separated from main-sequence stars, due to their relative abundance and ease of identification, as they are individually resolved from their host star. At present, there are $>$ 175 known companion benchmark brown dwarfs cataloged in the literature (see Faherty et al. 2010; Deacon et al. 2014; Rothermich et al. 2023). To understand the particular benefits of benchmark brown dwarfs, we can look to studies that have shown how empirical constraints can test current atmospheric and evolutionary models. For example, Burningham et al. (2009) presented the discovery of Wolf 940B, a T8.5 companion to the M4 dwarf, Wolf 940. In this work, they were able to take robust measurements for distance, metallicity, and age from the primary and apply these to the secondary T-dwarf companion to test model repeatability with a set of solar metallicity BT-Settl models (Allard et al. 2003). They found that the models underestimated the flux peak in the K spectral band, resulting in an overestimated model temperature of $\sim$100 K. They also showed that, at the time, non-solar metallicity model spectra did not agree well with observed data for late T dwarfs. With benchmark systems involving FGK-type primaries, we can even more precisely use inferred chemical properties from the primary (metallicity and abundance) to examine UCD atmospheric and evolutionary models, such as in the works of Bowler et al. (2009), Mann et al. (2013), Line et al. (2015), and Wang et al. (2022).

These works have been able to point out incongruities—or alternatively, consistencies—between observed data and spectral and evolutionary models, so that we may understand and tweak our underlying theoretical physical assumptions accordingly. While spectral or evolutionary analysis on non-benchmark brown dwarfs can also shed light on model precision, it is much more challenging to pinpoint the cause of poor matches when there are no certain constraints. This remains the significant motivation for studying benchmark brown dwarfs.

2.1. The Compositional Benchmark Sample

Of the collection of co-moving benchmark brown dwarfs, the main employment of known empirical properties is done through posterior comparison to resulting model values. While this is a useful comparative tool, it can also leave us with more open questions when known and model values are not within statistical agreement. As discussed above, this has been done in Burningham et al. (2009) to comment on and test model reproducibility of known spectral features. More recently, it has been used in the work of Line et al. (2015), Kitzmann et al. (2020), Calamari et al. (2022), which all utilized versions of retrieval methods (see Line et al. 2015; Burningham et al. 2017; Mollière et al. 2020, etc.) to analyze the observed spectra of Gl 570D and HD 3651B (Burgasser et al. 2006; Mugrauer et al. 2006), Epsilon Indi Bab (King et al. 2010) and Gl 229B (Nakajima et al. 1995; Oppenheimer et al. 1995), respectively, and determine the highest-likelihood fundamental parameters (i.e., molecular abundances, $T_{\rm eff}$, log(g), [M/H], etc.). To varied statistical degrees, what was reported in these studies was an inconsistency between the retrieved metallicity and carbon-to-oxygen (C/O) ratio of the companion and that known for its stellar host.

This application of benchmark data has proven to be a powerful tool in examining and challenging the assumptions we might have about a particular system. Specifically, in Calamari et al. (2022), the retrieved carbon and oxygen abundances in Gl 229B were compared to those reported for its primary, revealing that Gl 229B appeared to be comparatively oxygen depleted ($\approx 3\sigma$ disagreement). While there are a few ways of interpreting this result—most notably that the nascent origins of these two companions are inherently different—Calamari et al. (2022) concluded that this discrepancy, in part, was suggestive of misunderstood cloud chemistry in the modeling and theoretical estimations. It is important to note that only carbon and oxygen abundances for Gl 229A were readily available for comparative use in this system. However, this alone provided insight and motivation to re-examine the ways in which we model brown dwarf atmospheres and account for clouds.

To fully utilize companion benchmarks in our modeling requires systems in which a wider range of atomic abundances are readily available. To predict the condensate species and cloud particle density, we need a picture of the chemical landscape beyond just carbon and oxygen. Specifically, we want to know the abundances of the dominant reactive metal species (Mg, Si, Al, and Ca), to determine what kinds of clouds we would expect to see if the UCD companion did, in fact, contain the same elemental abundances as its stellar companion. While most co-moving brown dwarfs are found orbiting M-dwarf stars (Faherty et al. 2010; Deacon et al. 2014), it is notoriously difficult to calculate atomic abundances for stars of this spectral type, due to substantial molecular absorption bands throughout their spectra. As a result, we turn to benchmark systems in which the primary star is of spectral type F, G, or K, in hopes of attaining such chemical information.

While there have been several individual discoveries and compiled samples of benchmark brown dwarfs (e.g., Pinfield et al. 2006; Bowler et al. 2009; Burningham et al. 2009; Faherty et al. 2010; Deacon et al. 2014; Rothermich et al. 2023), here we conduct a thorough literature search for all brown dwarfs co-moving with an F, G, or K primary. While this criterion significantly limits the sample size, as more than half of all known co-moving brown dwarfs are companions to objects of spectral type M or later, we do this to prioritize the availability and accuracy of stellar atomic abundances. In Section 1, we list all known and newly discovered brown dwarfs co-moving with an F, G, or K primary star, labeling this subset as the brown dwarf compositional benchmark sample. It is important to note that, in classifying compositional benchmarks, attention has been taken to isolate secondaries that are members of unresolved binaries, as disentangling their combined light spectra is a nontrivial task and can complicate analysis. One example of this type of system would be Gl 417 BC, which is a spectroscopically unresolved L4.5 + L6 brown dwarf binary co-moving with the G2 dwarf Gl 417 (Kirkpatrick et al. 2001; Dupuy et al. 2014). However, as there is an increased binary frequency among widely separated brown dwarfs with stellar-type primaries (Burgasser et al. 2005a), we include these here for completeness.

3. The Role of L-Type Dwarfs in Benchmarking

At the ultracool end of the spectral sequence, the L, T, and Y dwarfs exhibit spectra filled with large molecular absorption bands and atmospheres cool enough to form clouds. Of the 57 systems in the compositional benchmark sample listed in Table 1, $\sim$75% are systems in which the UCD companion is an L-type dwarf, a spectral classification bounded by 1300 $< T_{\rm eff} <$ 2200 K. This statistic is likely due to an observational bias, as L dwarfs in the local region will be brighter, and

Table 1
The Compositional Benchmark Sample

Object	Primary	R.A.	Decl.	SpT Secondary	SpT Primary	$d_{\rm Primary}$ (pc)	Separation (arcsec)	Proj. Sep (AU)	Age (Gyr)	References
Known Systems										
2MASS J00193275 + 4018576	LP 192-58	4.8859931	40.3151441	L2	K7	55.21 ± 0.11	58.5	3990	0.3–10	1, 2
2MASS J00302476 + 2244492	BD+21 55	7.6042199	22.7461537	L0.5	K2	37.91 ± 0.14	117.1	3970	0.5–10	1, 2
HD 3651 B	HD 3651	9.829614	21.254559	T7.5	K0.5V	11.14 ± 0.01	43	480	0.7–4.7	1, 2, 8, 9, 23
HD 4113 C	HD 4113	10.8025	−37.9826306	T9	G5V+M1V	41.92 ± 0.09	0.535	22	3–6	27
HD 4747 B	HD 4747	12.361505	−23.212463	L/T	G8/K0V	18.85 ± 0.01	0.61	10	0.9–3.7	18
ULAS J014016.91 + 015054.7	BD+01 299	25.071311	1.8484382	T5	K5	38.56 ± 0.03	31	35–45	6.5–13.5	3, 12
2MASS J01591078 + 3312313	HD 12051	29.7959843	33.207192	L6	G9V	24.77 ± 0.02	52.1	1300	2.2–10.2	1, 2
HD 13724 B	HD 13724	33.086156	−46.816377	T4	G3/5V	43.48 ± 0.06	0.24	26.3	0.05–1.5	26
2MASS J02233667 + 5240066	HD 14647	35.902796	52.668514	L1.5	F5	80.41 ± 0.46	47.7	3300	0.5–2.4	2
2MASS J02355993-2331205	HD 16270	39.00019195	−23.52224277	L1	K2.5Vk	21.22 ± 0.02	11.95	250	<1	1, 3
HD 19467 B	HD 19467	46.827	−13.762028	T5.5	G3V	32.03 ± 0.02	1.6	51	4–10	13
HIP 21152 B	HIP 21152	68.019917	5.409944	L/T	F5V	43.21 ± 0.05	408	17.5	0.65–0.85	1, 29
HD 33632 Ab	HD 33632 Aa	78.3208	37.2808	L9.5	F8V	26.39 ± 0.02	0.75	20	1.2–4.5	19
2MASS J05394952 + 525352	HD 37216	84.9566683	52.8992533	L5	G5V	28.08 ± 0.04	27	753	1.1–9.3	1, 2
2MASS J06135342 + 1514062	HD 253662	93.4725944	15.234332	L0.5	G8IV	86.46 ± 0.34	20.1	> 1252	< 10	1, 2
AB Pic B	AB Pic	94.804162	−58.055611	L1	K1V	50.14 ± 0.03	5.5	250–270	0.03	1, 16, 23
2MASS J06324849 + 5053351	LSPM J0632 + 5053	98.202075	50.893106	L1.5	G2	82.58 ± 0.13	47.4	4499	0.2–10	2
2MASS J06462756 + 7935045	HD 46588	101.6121946	79.5818179	L9	F7V	18.21 ± 0.04	79.2	1420	1.3–4.3	1, 2
HD 47197 B	HD 47197	102.339167	43.759194	L4	F5V	41.47 ± 0.05	0.8	43	0.26–0.79	1, 15
2MASS J07580132-2538587	HD 65486	119.5073205	−25.6508698	T4.5	K4Vk	18.48 ± 0.01	88	1630	0.3–2.8	1, 2
eta Cnc B	eta Cnc	128.132502	20.449967	L3.5	K3III	97.48 ± 0.83	2.2–3.5	154	15000	1, 17
HD 72946 B	HD 72946	128.963611	6.62277	L5	G8V	25.87 ± 0.08	6.5	10	1–2	1, 28
2MASS J10221489 + 4114266	HD 89744	155.5623583	41.2457764	L0	F7V	38.68 ± 0.11	2460	63	1.5–3	1, 2, 23
2MASS J11102921-2925186	CD-28 8692	167.621714	−29.4221669	L2	K5V	39.79 ± 0.07	50.8	2026	9.5–13.5	1, 25
2MASS J12173646 + 1427119	HD 106888	184.4015804	14.4531479	L1	F8	67.18 ± 0.57	38.1	2170	0.3–2.5	1, 4
WISE J124332.17 + 600126.6	BD+60 1417	190.88386	60.023957	L8γ	K0	44.96 ± 0.03	37	1662	0.01–0.15	11
2MASS J13005061 + 4214473	BD+42 2363	195.2084201	42.246548	L1	K6V	44.15 ± 0.06	132.8	5640	0.3–10	1, 2
GJ 499 C	GJ 499 AB	196.420872	20.7779818	L4	K5+M4	19.65 ± 0.02	516	9708	3–5	1, 5
2MASS J13204427 + 0409045	HD 116012	200.1820776	4.1522243	L5	K0V	30.31 ± 0.046	516	9708	12–14	1, 5
ULAS J13300249 + 0914321	TYC 892-36-1	202.5102524	9.2422718	L2	K-type	246.85 ± 2.80	260.4	...	0.2–1.5	1, 4
2MASS J13324530 + 7459441	BD+75 510	203.188635	74.995628	L2	K8	35.40 ± 0.01	38.3	1364	0.2–1.4	5
HD 118865 B	HD 118865	204.9323213	1.0766982	T5	F7V	60.80 ± 0.20	148	9200	1.5–4.9	1, 2
2MASS J14165987 + 5006258	HD 125141	214.2474598	50.1080132	L4	G5	47.11 ± 0.06	570	...	8.5–11	1, 34
ULAS J142320.79 + 011638.2	HD 126053	215.8371027	1.276492	T8	G1.5V	17.44 ± 0.01	152.8	2630	2.3–14.4	1, 33
2MASS J14284235-4628393	CD-45 9206	217.1761684	−46.4784943	T4.5	K7Vk	24.07 ± 0.02	377.3	9000	1–5	1, 7
HD 130948 BC	HD 130948	222.566667	23.911611	L2+L2	G2V	18.20 ± 0.01	2.64	46.5	0.4–0.9	20, 21
GJ 570 D	GJ 570	224.3175381	−21.3712191	T7	K4V	5.88 ± 0.002	261.7	1525	2–10	1, 10, 23
ULAS J150457.65 + 053800.8	BD+06 2986	226.2388579	5.632459	T6	K8V	19.02 ± 0.02	63.8	1230	> 1.6	1, 2
2MASS J15232263 + 3014562	* eta CrB	230.8449168	30.2481943	L8	G2V+G2V	17.86 ± 0.25	195.3	3635	3–5	6
2MASS J17262235-0502110	* 47 Oph	261.59315	−5.0364	L5.5	F3V*	32.27 ± 0.16	294.1	1890	1.6–1.9	2
2MASS J18005854 + 1505198	HD 164507	270.2436883	15.08842874	L1	G5IV	45.44 ± 0.07	25.5	1136	3–4	1, 25
HR 7672 B	HR 7672	301.025833	17.070278	L4	G0V	17.77 ± 0.01	0.79	14	1–3	1, 22
HD 203030 B	HD 203030	319.74572	26.22948	L7.5	K0V	39.29 ± 0.09	11	487	0.13–0.4	1, 2, 6, 23
2MASS J21442847 + 1446077	V* HN Peg	326.1198745	14.7683382	T2.5	G0V+	18.13 ± 0.02	42.9	795	0.1–0.5	1, 8, 23
ϵ Indi Bab	ϵ Indi	331.0767776	−56.793953	T1.5+T6	K5V	3.64 ± 0.003		1459	0.8–2.0	1, 14, 23

Table 1
(Continued)

Object	Primary	R.A.	Decl.	SpT Secondary	SpT Primary	$d_{\rm Primary}$ (pc)	Separation (arcsec)	Proj. Sep (AU)	Age (Gyr)	References
2MASS J22461844 + 3319304	BD+32 4510	341.576865	33.325119	L1.5	K2*	64.68 ± 3.23	16	1040	0.1–10	2
Newly Discovered Systems										
CatWISE J005635.48-240401.9	HIP 4417	14.1478506	−24.0672083	L8	K0	67.60 ± 0.08	102	6924	...	1, 24
CatWISE J030005.73-062218.6	BPS CS 22963-0014	45.0238923	−6.371848	L9	K7	67.13 ± 0.08	63	4200	...	1, 24
CatWISE J055909.00-384219.8	HD 40781	89.787502	−38.7055027	L4	G0V	60.65 ± 1.30	54.5	3259	< 1	1, 24
CatWISE J065752.45 + 163350.2	HD 51400	104.46857	16.563966	L6	G5	37.08 ± 0.78	64	2254	...	1, 24
CatWISE J085131.24-603056.2	PM J08515-6029	132.8801846	−60.5156128	L3	K7	30.93 ± 0.01	95.3	2948	< 1	1, 24
CatWISE J133427.70-273053.1	HD 117987	203.61543	−27.514766	L0	K3V	36.95 ± 0.46	50	1772	...	1, 24
CatWISE J183207.94-540943.3	HD 170573	278.03311	−54.162028	T7	K4.5Vk	19.12 ± 0.01	619.3	11843	9–13.5	1, 24
Known Unresolved Binaries										
2MASS J00250365 + 4759191	HD 2057	6.2669728	47.9877566	L4+L4	F8	54.01 ± 0.40	210	8800	< 1	32
HD 8291 B	HD 8291	20.5708829	3.522572	L1+T3	G5V	50.38 ± 0.35	44.9	2570	0.5–10	1, 2
Gl 337 CD	Gl 337	138.0584919	14.9956706	L8.5+L7.5	G8V+K1V	20.35 ± 0.14	43	881	0.6–3.4	1, 31
Gl 417 BC	Gl 417	168.1055653	35.8028953	L4.5+L6	G2	22.65 ± 0.02	90	2000	0.08–0.3	1, 30

References. (1) Gaia Collaboration et al. 2021; (2) Deacon et al. 2014; (3) Burningham et al. 2018; (4) Marocco et al. 2017; (5) Gomes et al. 2013; (6) Pinfield et al. 2006; (7) Lodieu et al. 2014; (8) Luhman et al. 2007; (9) Mugrauer et al. 2006; (10) Burgasser et al. 2000; (11) Faherty et al. (2021) ; (12) Skrzypek et al. 2016; (13) Crepp et al. 2012; (14) Liu et al. 2010; (15) Metchev & Hillenbrand 2004; (16) Chauvin et al. 2005; (17) Zhang et al. 2010; (18) Crepp et al. 2016; (19) Currie et al. 2020; (20) Dupuy et al. 2009; (21) Potter et al. 2002; (22) Liu et al. 2002; (23) Faherty et al. 2010; (24) Rothermich et al. 2023; (25) Marocco et al. 2020; (26) Rickman et al. 2020; (27) Cheetham et al. 2018; (28) Maire et al. 2020; (29) Kuzuhara et al. 2022; (30) Kirkpatrick et al. 2000; (31) Wilson et al. 2001; (32) Reid et al. 2006; (33) Pinfield et al. 2012; 34. Chiu et al. 2006.

therefore easier to identify, than T or Y dwarfs. However, this bias works in our favor, in regard to calibrating and tuning atmospheric modeling of brown dwarfs, due to the particularly cloudy photospheres of L dwarfs (Burningham et al. 2017; Suárez & Metchev 2022; Vos et al. 2023).

Calamari et al. (2022) showed that the population of brown dwarfs modeled with retrievals have an anomalously high median C/O ratio (∼0.79), which is shown to be inconsistent with the solar neighborhood, where the median C/O ratio for local F, G, and K-type dwarfs is ∼0.47 (Brewer et al. 2016). While we could consider that this is a real attribute of this sample of brown dwarfs, the uniformly oxygen-depleted atmospheres suggest a systematic modeling error in the way clouds are accounted for, as oxygen-rich condensates are known to play a major role in atmospheres < 2200 K. Within the substellar population, the most abundant object choices for evaluating the influence of clouds are L and T dwarfs. T dwarfs are the simpler objects to approach, given the relative lack of silicate clouds in the photosphere and dominance of methane gas. However, for the examination of oxygen sequestration and condensate species formation, it is useful to examine the more complex photospheres of L dwarfs.

A notable feature of UCD atmospheres is condensate formation, not only theorized to exist (e.g., Lunine et al. 1986; Tsuji et al. 1996; Marley et al. 1999; Ackerman & Marley 2001; Lodders 2002, 2004; Kirkpatrick 2005), but also evidenced in observable mid-infrared spectra (Cushing et al. 2006; Suárez & Metchev 2022). As described in Kirkpatrick (2005), early L dwarfs near the M/L transition see the spectral line disappearance of TiO and VO, as those molecules are sequestered into oxygen-bearing condensates (e.g., $CaTiO_3$, $Ca_4Ti_3O_{10}$, $Ca_3Ti_2O_7$, Ti_2O_3, Ti_3O_5, and Ti_4O_7). Related to titanium condensate chemistry are aluminum and calcium, which form condensates (i.e., Al_2O_3, $CaAl_{12}O_{19}$, $CaAl_4O_7$, and $Ca_2Al_2SiO_7$) at slightly higher temperatures than titanium, but similarly impact the availability of oxygen (Burrows & Sharp 1999; Allard et al. 2001; Lodders 2002; Lodders & Fegley 2002; Wakeford et al. 2017).

A similar phenomenon occurs with iron, magnesium, and silicon at the transition into the mid-L (L4–L6) regime. The FeH and CrH absorption features that shape early- to mid-L spectra begin to weaken with the appearance of iron and magnesium-silicate clouds—most notably, forsterite (Mg_2SiO_4) and enstatite ($MgSiO_3$), the Mg-rich endmembers of olivine and pyroxene, respectively (Burrows & Sharp 1999; Lodders & Fegley 2002, 2006; Lodders 2010; Visscher et al. 2010a). Mid-infrared observational evidence of this silicate cloud feature is cataloged in the work of Suárez & Metchev (2022), who measured the strength of silicate absorption at 8–11 μm in 69 L dwarfs across spectral types L0–L8. They found evidence for silicate clouds across the L spectral sequence, while also noting that this feature disappears upon entering the T spectral type (around T2). Despite theoretical predictions of photospheric alkali metal (KCl and Na_2S) and sulfide (MnS and ZnS) clouds in T dwarfs (e.g., Morley et al. 2012), they generally exhibit cloudless photospheres with the potential for the same silicate clouds to be forming in deeper, unobservable parts of the atmosphere (see Kirkpatrick 2005; Line et al. 2015, 2017; Calamari et al. 2022).

Accordingly, if we want to understand and accurately model the chemistry of UCDs, we must first understand the thermochemical processes behind condensate (i.e., cloud) formation. In order to check these thermochemical cloud predictions, a useful starting point is studying L-dwarf spectra where we can test theory against observation, making L-dwarf chemical benchmarks a prime target of study.

Table 2
Abundance Ratios of Selected Compositional Benchmark Primaries

Name	C/O	Mg/Si	Ca/Al	References
HD 12051	0.513	1.030	0.668	1
HD 203030	0.468	0.939	1.011	1
HD 46588	0.447	0.984	1.083	1
HD 126053	0.426	1.030	0.653	1
HD 19467	0.363	1.129	0.543	1
HD 37216	0.479	0.918	0.822	2
HD 164507	0.380	1.104	0.785	2
HD 3651	0.501	1.030	0.623	2
HD 4747	0.426	1.054	0.803	1
HD 33632	0.398	1.079	0.803	2
HD 130948	0.490	0.984	1.131	1
HR 7672	0.549	1.054	0.767	1

References. (1) Brewer et al. 2016; (2) Rice & Brewer 2020.

4. Sample Selection

In exploring well-characterized systems, we began by cross-matching our compositional benchmark sample with published elemental abundance studies for main-sequence stars (e.g., Adibekyan et al. 2012; Brewer et al. 2016; Delgado Mena et al. 2021) in search of a host companion with well-characterized chemistry. We prioritized literature spectroscopic chemical abundance studies of main-sequence stars that had a uniform observational and/or reduction setup, to minimize systematics that could contaminate the analysis. We found that Brewer et al. (2016) and Rice & Brewer (2020) were inclusive of our sample and produced robust measurements for temperature, gravity, metallicity, and abundance over a large sample (> 2000) of main-sequence stars. Both works utilized high-resolution ($R\sim$70,000), high signal-to-noise (S/N $\geqslant$ 200) HIRES spectra from the Keck I telescope. In Brewer et al. (2016), one-dimensional (1D) local thermodynamic equilibrium (LTE) models were iteratively fit to observed spectra using the procedure described in Brewer et al. (2015). Rice & Brewer (2020) added to this work by using *The Cannon*, a machine-learning technique (Ness et al. 2015; Casey et al. 2016), to build a well-characterized model trained on the data set from Brewer et al. (2016) that was shown to efficiently obtain high-precision stellar parameters with improved speed and accuracy. Both of these studies combined provide a uniform and reliable catalog of stellar parameters and abundances from which we base our study.

In Table 2, we outline the compositional benchmarks whose primaries have been thoroughly studied in either Brewer et al. (2016) or Rice & Brewer (2020), a total of 12 stars. We use the procedure outlined in Brewer & Fischer (2016) to convert from reported [X/H], the $\log_{10}$ of the solar relative number abundance of an element with respect to hydrogen, to abundance ratios for a given pair of elements:

$$X_1/X_2 = 10^{([X_1/H]-(X_1/H)_\odot)-([X_2/H]-(X_2/H)_\odot)}. \quad (1)$$

We do this for [C/H], [O/H], [Mg/H], [Si/H], [Ca/H], and [Al/H] to determine C/O, Mg/Si, and Ca/Al abundance ratios. Additionally, we examine these elemental abundances along with [Ti/H] and [V/H] as required inputs of the

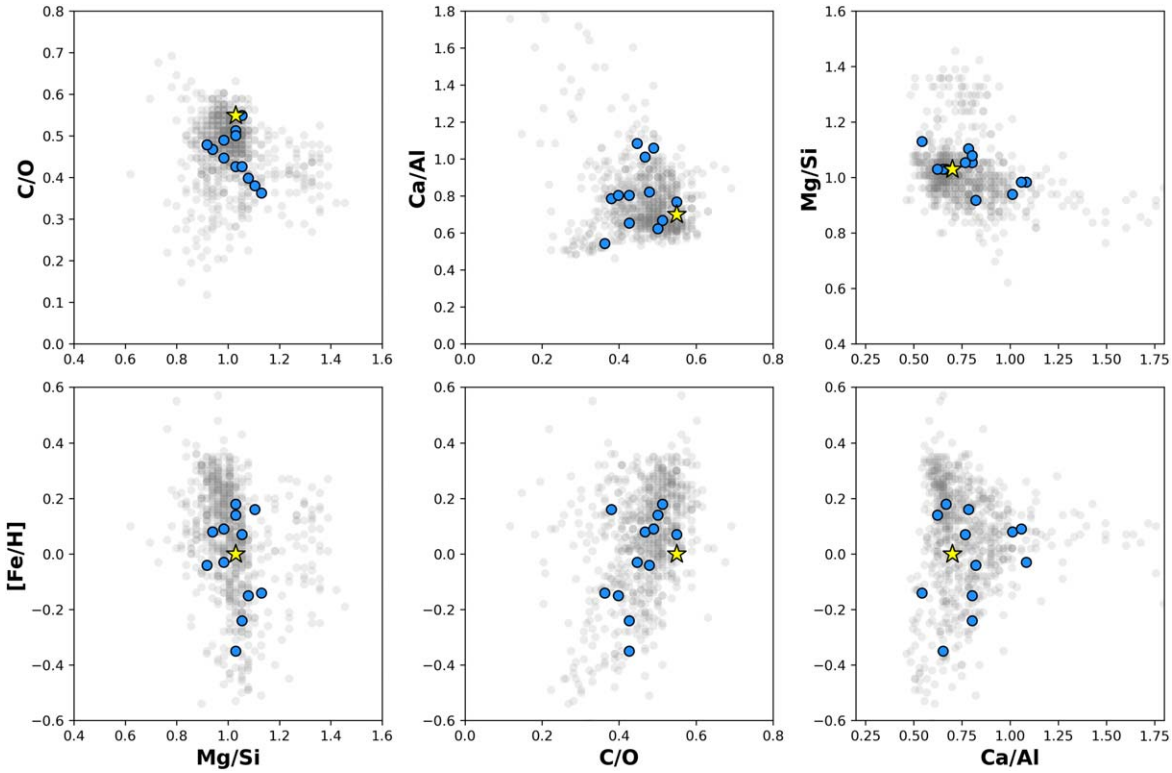

Figure 1. Highlighting the abundance ratios of the compositional benchmarks found in the Brewer et al. (2016) and Rice & Brewer (2020) stellar abundances catalogs. Blue points represent the compositional benchmarks laid out in Table 1, while the yellow star indicates solar abundance ratios. The gray points show the chemical variance in solar neighborhood FGK stars from Brewer et al. (2016).

thermochemical equilibrium procedures detailed in Section 6. We use the solar elemental abundances published in Lodders (2021).

While we highlight this intersection of known compositional benchmarks with elemental abundances from Brewer et al. (2016) and Rice & Brewer (2020) (12 stars), we use the data set from Brewer et al. (2016) with a cutoff for stars $\leqslant 100$ pc (746 stars) as a guide for the kind of chemical distributions we might expect to find across the solar neighborhood. In Figure 1, we show abundance ratios for C/O, Mg/Si, and Ca/Al for the compositional benchmark subset and the Brewer et al. (2016) solar neighborhood sample plotted against each other as well as overall metallicity, traced by [Fe/H], to outline the range of local chemical abundances on which we focus our discussion.

5. Review of Observational Brown Dwarf Spectral Signatures

In this section, we review the spectral absorption features for brown dwarfs that have served as observational evidence for the predicted thermochemistry in these atmospheres. These features establish the available data that can be translated into the calculations of fundamental parameters, such as C/O ratio and metallicity, in retrieval studies for these objects.

5.1. Major Absorbing Elements in Ultracool Dwarf Atmospheres

As established in the foundational works of Tsuji (1964), Lunine et al. (1986), Burrows et al. (1997), Allard et al. (1997), Marley et al. (1999), Burrows & Sharp (1999), Lodders (1999, 2002), Lodders & Fegley (2002), Geballe et al. (2002), Lodders & Fegley (2006), Kirkpatrick (2005), Lodders (2010), and Visscher et al. (2010a), the atmospheres of UCDs, and their subsequent spectra, are dominated by C, N, O, Ti, V, Fe, Cr, and neutral alkali element chemistry. At temperatures starting near the M/L spectral transition and cooler ($\leqslant 2200$ K), we see atomic and neutral atom absorption shift toward broadband molecular absorption features due to H_2O, CO, CO_2, CH_4, NH_3, FeH, TiO, VO, CrH, H_2S, and HCN throughout the optical and infrared (see Burgasser et al. 2002; Geballe et al. 2002; Marley et al. 2002; Kirkpatrick 2005; Cushing et al. 2006; Faherty et al. 2014; Helling & Casewell 2014). Retrieval models attempt to constrain the abundances of these absorbers across spectral type—for L dwarfs, mainly H_2O, CO, CO_2, CH_4, FeH, VO, TiO, CrH, Na, and K; for T dwarfs, H_2O, CO, CH_4, CO_2, NH_3, Na, and K; and for Y dwarfs, H_2O, CO, CO_2, CH_4, NH_3, and PH_3. To date, several retrieval studies have been able to constrain abundances of major absorbers (i.e., H_2O, CO, CH_4, NH_3, Na, and K) in both L, T, and early Y dwarfs (e.g., Line et al. 2017; Zalesky et al. 2019, 2019, 2022; Burningham et al. 2021; Calamari et al. 2022), with some studies on L dwarfs having shown abundance constraints on minor metal hydrides and oxides (FeH, VO, and TiO) as well (Burningham et al. 2017, 2021; Vos et al. 2023).

In this subsection, we provide a brief overview on the dominant thermochemistry in the L, T, and Y temperature regimes marked by the most abundant volatile elements (H, C, N, and O), as these resulting species drive the C/O ratio and metallicity solutions in current retrieval modeling. We focus our discussion on thermochemical equilibrium assumptions for well-mixed, convective atmospheres as a necessary simplification in our modeling. For a more detailed discussion, see Lodders & Fegley (2002).

Carbon and Oxygen. The most identifiable features in UCD spectra often result from carbon and oxygen chemistry in the form of H_2O, CH_4, CO, and CO_2. In warmer, less dense atmospheres (i.e., L-dwarf atmospheres), we expect to see more carbon and oxygen in CO and CO_2, whereas cooler, denser atmospheres (i.e., T- or Y-dwarf atmospheres) would show more CH_4 and H_2O. We can consider CO_2 to play a lesser role under thermochemical equilibrium assumptions, as it is expected to be observable at much lower pressures ($\log P$ (bar) < -8) than the photospheric pressures we probe ($1 < \log P$ (bar) < 10). For the remaining three major absorbers, they are governed by the net thermochemical reaction:

$$CO + 3H_2 \rightleftharpoons CH_4 + H_2O. \quad (2)$$

It is important to note that, even in a CO-dominated atmosphere, the abundances of CH_4 and H_2O do not drop to zero, and vice versa. Lodders & Fegley (2002) also discuss the implication that overall metallicity ([Fe/H]) has on the $CH_4 = CO$ boundary (i.e., the threshold in $P - T$ space between a CO- or CH_4-dominated atmosphere). As metallicity decreases, the $CH_4 = CO$ boundary shifts to higher temperatures, whereas as metallicity increases the $CH_4 = CO$ boundary shifts to lower temperatures. Additionally, while CO_2 is not considered a major C-bearing gas in these atmospheres, it is moderately abundant ($-12 < \log X_{CO_2} < -6$) in a CO-dominated atmosphere. Observational evidence for this species exists in hotter L-dwarf atmospheres, but subsequent retrieval modeling attempts have failed to constrain its relatively low abundance (e.g., Line et al. 2015; Gonzales et al. 2020), and as such, is not considered a major contributor in determining C/O ratios for brown dwarfs.

While we focus our analysis in Section 7 on thermochemical equilibrium assumptions, we do have observational evidence of chemical disequilibrium for the CO-to-CH_4 conversion (i.e., Noll et al. 1997; Oppenheimer et al. 1998; Miles et al. 2020) in brown dwarf atmospheres. This results in higher observed abundances of CO than predicted by thermochemical equilibrium, due to rapid vertical mixing from the deeper, hotter atmosphere at rates faster than the chemical timescale conversion to CH_4 (Prinn & Barshay 1977; Fegley & Lodders 1996; Lodders & Fegley 2002; Visscher et al. 2006; Visscher & Moses 2011). While this is a real, observed phenomenon, we focus here on thermochemical equilibria for well-mixed atmospheres.

For the CO-to-H_2O conversion, even in the regime where CO is the major C-bearing gas, half of all oxygen can still be in H_2O, as oxygen is nearly twice as abundant as carbon. It is important to note, as discussed for a solar-composition gas in Lodders & Fegley (2002), that the distribution of oxygen atoms between H_2O and CO in a UCD atmosphere is going to be affected by the production of oxygen-rich clouds. We discuss theoretical implications of this further in Section 5.2.

Under equilibrium conditions for pressure and temperature expected in UCD atmospheres ($-4 < \log P$ (bar) < 3; $250 < T$ (K) < 2500), H_2O, CO, CH_4, and CO_2 will be the most abundant carbon- and oxygen-bearing species. Several other species exist within either CH_4- or CO-dominated atmospheres and may play key roles in H-C-N-O reaction kinetics (i.e., CH_3, C_2H_6, CH_2O, and CH_3OH), but their relative abundances and the strengths of their absorption lines are too weak to consider and have never been recovered in a spectral analysis.

Nitrogen. The other major contributor shaping UCD spectra comes from the distribution of nitrogen in NH_3. Similar to the carbon and oxygen chemistry above, nitrogen chemistry in these atmospheres is governed by the net thermochemical reaction:

$$0.5N_2 + 1.5H_2 \rightleftharpoons NH_3. \quad (3)$$

In cooler, denser atmospheres, NH_3 gas dominates, while N_2 gas dominates in warmer, less dense atmospheres. Similarly to the $CH_4 = CO$ boundary, the overall metallicity impacts the boundary temperature. As metallicity decreases, the $NH_3 = N_2$ boundary shifts to higher temperatures, whereas as metallicity increases, the $NH_3 = N_2$ boundary shifts to lower temperatures. As discussed for the carbon and oxygen chemistry, an N_2-dominated atmosphere still has a nonzero abundance of NH_3. It is relevant to note here that any object showing NH_3 absorption in its spectrum is expected to have CH_4 as its major carbon-bearing species (Burrows et al. 2003; Canty et al. 2015; Line et al. 2017).

While condensation of N-bearing species into NH_3 and/or NH_4SH is possible in the coolest atmospheres (e.g., Jupiter and Saturn; Lewis 1969; Carlson et al. 1987; Lodders & Fegley 2006), these types of condensate clouds are not expected in the warmer atmospheres of L and T dwarfs and do not play a role in subsequent modeling.

As with the carbon chemistry, other minor N-bearing condensates are predicted to exist within either N_2- or NH_3-dominated atmospheres (i.e., CH_3NH_2 and HCN). As N_2 does not have absorption features in the near-infrared, its abundance cannot be constrained by observational data, and NH_3 then remains the only major N-bearing species able to be constrained through retrieval modeling. As a result, NH_3 is the only N-bearing species to contribute to metallicity calculations. This hinders our ability to quantify the total nitrogen budget in a given atmosphere.

5.2. Major Refractory Condensates

Beyond gaseous molecular absorption bands that shape brown dwarf spectra, we have theoretical and observational evidence of condensate absorption as mentioned in previous sections (see Section 3 and Section 5.1). Thermochemically derived condensation curves of many refractory mineral condensates overlap with the pressure and temperature profiles of UCDs, including $CaTiO_3$, Al_2O_3, Mg_2SiO_4, $MgSiO_3$, SiO_2, ferrous metal, Na_2S, Li_2S, LiF, KCl, and ZnS (Marley et al. 1999, 2002; Chabrier et al. 2000; Ackerman & Marley 2001; Lodders 1999, 2002; Lodders & Fegley 2002, 2006; Visscher et al. 2006, 2010a; Morley et al. 2012; Wakeford et al. 2017).

While the salt and sulfide clouds are expected in the observable photospheres of cooler T dwarfs, we have yet to find strong spectral evidence of these clouds using retrieval analysis. This could be due to a variety of reasons, including but not limited to clouds sinking below the photosphere in T dwarfs (e.g., Marley et al. 1996; Marley et al. 2013; Line et al. 2015; Zalesky et al. 2022; Calamari et al. 2022), or weak or nonexistent spectral absorption features in the near-infrared despite observed variance in infrared T-dwarf colors (Morley et al. 2012). In warmer objects, or in deeper, hotter layers in T dwarfs, we find the mineral oxide and atomic iron condensates. These condensates will form the most substantial cloud layers

in UCD atmospheres, due largely to the high relative abundance of magnesium, iron, and silicon.

Due to the relatively high condensation temperature of Fe metal, nearly all of this elemental reservoir is condensing into a cloud layer below the photosphere in L dwarfs. This limits Fe abundance above this cloud layer and prohibits it from being a major gaseous absorber (as FeH, FeOH, $Fe(OH)_2$, FeS, etc.; Allard et al. 1997; Burgasser et al. 2002; Burrows & Sharp 1999; Visscher & Fegley 2005; Lodders & Fegley 2006; Visscher et al. 2010a) or a major oxygen sink (as condensed $FeSiO_3$ or Fe_2SiO_4, iron endmembers of the pyroxene and olivine mineral groups, respectively; Visscher et al. 2010a). Moreover, the hydrogen-rich atmospheres of UCDs are expected to be too reducing (i.e., the oxygen fugacity is too low) to allow for any appreciable formation of Fe oxides or Fe silicates under equilibrium conditions.

Prior to the condensation points of forsterite (Mg_2SiO_4) and enstatite ($MgSiO_3$), the magnesium endmembers of the pyroxene and olivine mineral groups, corundum (Al_2O_3) and perovskite ($CaTiO_3$), will condense. This will lower the available oxygen inventory above these clouds, but as the abundances of calcium, aluminum, and titanium are roughly two to three orders of magnitude less abundant than oxygen, the impact on the oxygen inventory is minimal. This is true also for the calcium silicate species anorthite ($CaAl_2Si_2O_8$) and diopside ($CaMgSi_2O_6$) that are condensing in $P-T$ space nearer to forsterite and enstatite but are still limited by the total calcium and aluminum abundance, minimally contributing to the depletion of atmospheric oxygen. So, we are effectively left with condensates that are significant sources of oxygen sinks in UCD atmospheres: forsterite, enstatite, and quartz. At present, we have mid-infrared observational evidence of silicate condensate (Mg_2SiO_4, $MgSiO_3$, and SiO_2) absorption (Cushing et al. 2006; Burningham et al. 2021; Suárez & Metchev 2022; Grant et al. 2023); however, deciphering the exact species responsible remains a challenge.

In the following sections, we focus on the totality of these oxygen-rich condensate species (Mg_2SiO_4, $MgSiO_3$ and SiO_2, Al_2O_3, $CaTiO_3$, $CaAl_2Si_2O_8$, and $CaMgSi_2O_6$) not only because their existence is most feasibly modeled (e.g., Burningham et al. 2021; Vos et al. 2023) but because they directly tie in to the determination of oxygen abundance in UCD atmospheres. As oxygen abundance can be a potential formation and evolution tracer (see Öberg et al. 2011; Madhusudhan 2012), it is essential to understand the impact condensate formation has on oxygen sequestration and how we can most accurately account for this in our modeling.

6. Theoretical Framework for Thermochemical Analysis in Brown Dwarfs

One major assumption in the framework of current UCD atmospheric modeling is the use of solar abundance ratios as the standard for understanding the chemistry of these atmospheres beyond spectral line absorbers. These solar abundance ratios are used not only to disentangle the effects of condensate formation but also as population calibrators to help us ground the fundamental parameters of nearby brown dwarfs. However, we have already seen from the work of Brewer et al. (2016), as illustrated in Figure 1, that the solar C/O ratio lies at the higher end of the population of F, G, and K-type stars in the local solar neighborhood. This might suggest that using the solar C/O ratio as a chemical marker for the local brown dwarf population is an overestimation. As shown in Calamari et al. (2022), $>80\%$ of the current population of retrieved brown dwarfs has a C/O ratio greater than solar ($\sim$0.55 from Lodders (2021)), with $>40\%$ being greater than 0.8, a category of carbon-rich stars thought to be less than $\sim$1% of the local solar neighborhood (Brewer & Fischer 2016).

While abundance ratios are a useful trend guide, if we want to understand the chemical makeup of UCD atmospheres, it is more informative to examine actual elemental abundances (the occurrence of a given element relative to all other elements). We again point back to Calamari et al. (2022), where oxygen, specifically, appeared to be depleted in Gl 229B as compared to Gl 229A. While still an open question, this pinpoints what types of atmospheric, or even formation, dynamics could be causing such an outcome. If we want to explore this open question regarding oxygen in brown dwarfs, we turn not only to abundance ratios but individual element abundances. We know that the chemical makeup of the solar neighborhood does vary—in addition to using broad metrics like C/O ratio and metallicity ([Fe/H]), we want to know how specific element abundance may change and how that can impact subsequent cloud formation. Specifically, we look at species that act as potential oxygen sinks in UCD atmospheres (see Section 5.2).

6.1. Stellar Abundances as a Tool for Understanding Companion Atmospheres

By focusing on well-studied primary stars, we can examine the total chemical makeup of a given system by using observationally measured abundances of certain elements. Assuming co-evality, we can use the stellar abundances of both volatile and refractory elements to examine how oxygen is theoretically being sequestered into refractory condensates in a companion UCD atmosphere. This methodology works uniquely for compositional benchmark systems by utilizing known host star element abundances and assuming a similar chemical makeup for its companion. This assumption is strongly supported by the observation in our own Solar System that element abundances in the solar photosphere (with the exception of H and He) closely match the element abundances directly measured in the most primitive chondritic meteorites, widely thought to be the building blocks of the planets in our Solar System (Lodders 2021). While this introduces a new assumption, we use this method in order to revisit the calculation done in Burrows & Sharp (1999), where they employed solar abundances to predict that approximately 3.28 oxygen per silicon atom would end up in clouds (accounting for $\sim$14% of bulk oxygen). We address the implications and evaluations of our assumption in Section 8.

In order to constrain the amount of total oxygen that would sink into clouds for each benchmark system, we use the published abundances from Brewer et al. (2016) and Rice & Brewer (2020) to stoichiometrically calculate how much oxygen will bond with the refractory elements Mg, Si, Ca, Al, Ti, and V. Under thermodynamic equilibrium conditions, in cooler atmospheres, O-bearing condensates form at the transition from the deep interior to cooler pressure layers near the photosphere. In these calculations, we assume that the total bulk abundance of each of these refractory elements is bonding with oxygen, forming MgO, SiO_2, CaO, Al_2O_3, TiO_2, and VO. Subsequent refractory condensates (see Section 5.2) can be constructed from combinations of these metal oxides, making the quantitative oxygen sink path-independent—i.e., the

resulting phase composition(s) of the clouds are irrelevant. For example, enstatite and forsterite can be made by combining metal oxide building blocks via net thermochemical reactions:

$$MgO + SiO_2 \rightleftharpoons MgSiO_3 \quad (4)$$

$$2MgO + SiO_2 \rightleftharpoons Mg_2SiO_4, \quad (5)$$

wherein the total amount of oxygen that may be sequestered into Mg-silicates is determined by the available abundances of Mg and Si, and not upon the relative proportions of particular silicate phases. For a more in-depth discussion of how these various gaseous oxides form mineral condensates, see Lodders (1999, 2002, 2010), Ackerman & Marley (2001), Allard et al. (2001), Visscher et al. (2010a), and Wakeford et al. (2017).

If we consider these types of chemical pathways for both major (Mg and Si) and minor (Ca, Al, Ti, and V) refractory elements, we can determine a maximum oxygen sink fraction (the percent fraction of oxygen in condensate clouds) based upon oxidation stoichiometry (e.g., see Visscher & Fegley 2005):

$$\Sigma O_{cloud} = 2\Sigma Si + \Sigma Mg + \Sigma Ca + 1.5\Sigma Al + 2\Sigma Ti + \Sigma V \quad (6)$$

$$O_{sink} = \frac{\Sigma O_{cloud}}{\Sigma O}, \quad (7)$$

where ΣO_{cloud} is the total amount of oxygen taken into metal oxides (and thus condensate clouds), ΣO is the total amount of oxygen, and O_{sink} is the fraction of total oxygen in clouds in a given atmosphere. We note that, though titanium and vanadium are strong gaseous absorbers, they are typically present in trace ($\sim$1%) amounts in the most abundant mineral condensates. However, we include their abundances for completeness in our calculation.

The advantage of this stoichiometric approach is that the total oxygen removal is limited only by the abundances of the major refractory elements and does not require prior knowledge of the distribution of elements into specific condensate phases. While our determination of O_{sink} includes minor refractory elemental abundances (Ca, Al, Ti, and V), Mg and Si are responsible for $>$ 90% of the oxygen removal into such clouds. Moreover, the abundances of minor metals tend to increase with increasing abundances of Mg and Si. Using elemental abundances from the Brewer et al. (2016) solar neighborhood sample, we can thus make a first-order approximation for O_{sink} in companion objects using the Mg and Si abundances as a proxy for all metal oxides:

$$O_{sink} \approx 2.024(\Sigma Si/\Sigma O) + 1.167(\Sigma Mg/\Sigma O). \quad (8)$$

From this relation, the number of oxygen atoms removed per silicon atom (see Figure 2 and Burrows & Sharp 1999) can also be estimated:

$$O_{cloud}/\Sigma Si \approx 2.024 + 1.167(\Sigma Mg/\Sigma Si), \quad (9)$$

where $\Sigma Mg/\Sigma Si$ describes the bulk Mg/Si abundance ratio in the system. The significance of this ratio for silicate phase composition will be explored in Section 6.2.

We can also consider the impact of the oxygen sink on the observable C/O ratio, such that the removal of oxygen into condensed phases will cause the C/O ratio to become greater above the condensate cloud layers relative to the "below-cloud" (i.e., bulk atmosphere) C/O ratio. This "above-cloud," or observed, C/O ratio can be expressed by

$$(C/O)_{obs} = (C/O)_{bulk} \times \frac{1}{1 - O_{sink}}, \quad (10)$$

where $(C/O)_{obs}$ is the observed C/O ratio in the upper atmosphere, $(C/O)_{bulk}$ is the bulk atmospheric C/O ratio, and O_{sink} is the percent fraction of oxygen sequestered in clouds, calculated from Equation (7).

By substitution of O_{sink} (Equation (8)) into Equation (10), the $(C/O)_{obs}$ ratio can be estimated from the bulk elemental abundances for C, O, Mg, and Si:

$$(C/O)_{obs} \approx \frac{\Sigma C}{\Sigma O - 2.024\Sigma Si - 1.167\Sigma Mg}. \quad (11)$$

Moreover, the observed abundance trends for ΣMg, ΣSi, ΣO, and the C/O ratio in the Brewer et al. (2016) solar neighborhood sample were used to derive a more general relationship for finding $(C/O)_{obs}$. From this sample, the abundances of Si and Mg can be roughly approximated by $(\Sigma Si/\Sigma O) \sim 0.1159(\Sigma C/\Sigma O)$ and $(\Sigma Mg/\Sigma O) \sim 0.1165(\Sigma C/\Sigma O)$. Substitution into the above expression thus yields

$$(C/O)_{obs} \approx \frac{(C/O)_{bulk}}{1 - 0.371(C/O)_{bulk}}, \quad (12)$$

which allows for estimates of the $(C/O)_{obs}$ ratio using only the bulk $(C/O)_{bulk}$ ratio. This expression can likewise be used to estimate bulk C/O, based upon *observed* values of the C/O ratio by accounting for the sequestration of oxygen into major condensate phases.

6.2. Classifying Major Condensates

In addition to determining the total percentage of oxygen in condensate clouds, we can also use the element abundances and abundance ratios of refractory elements to predict the type of oxygen-bearing clouds we might expect to see and model in a given atmosphere. Similar to the path-independent, stoichiometric calculations above, we can evaluate the silicate condensate sequence by a series of stoichiometric and mass-balance calculations.

Due to the high relative abundance of magnesium and silicon (as compared to calcium, aluminum, titanium, or vanadium), the dominant oxygen-bearing condensates in UCD atmospheres are expected to be the well-known "silicates": enstatite ($MgSiO_3$), forsterite (Mg_2SiO_4), and quartz (SiO_2). The inventories of these condensates will be affected (1) by the bulk abundances of their constituent elements (Mg and Si) and also (2) by the abundances of the minor refractory elements (Ca, Al, Ti, and V), as these elements will condense into even more refractory oxygen-bearing clouds deeper in the atmosphere and can thus affect the available, "above-cloud" inventory of Mg or Si.

A solar-composition gas will condense magnesium and silicon mostly into enstatite, forsterite (and possibly quartz, see below) with $<$ 20% of Mg or Si into minor refractory condensates (see Lodders 2002; Visscher et al. 2010a). However, to illustrate the silicate condensation sequence, we first consider a solar-composition gas where forsterite and enstatite are the *only* Mg- and Si-bearing condensates. We can thus determine the inventory of forsterite by the following:

$$\Sigma Mg = 2A_{Mg_2SiO_4} + A_{MgSiO_3} \quad (13)$$

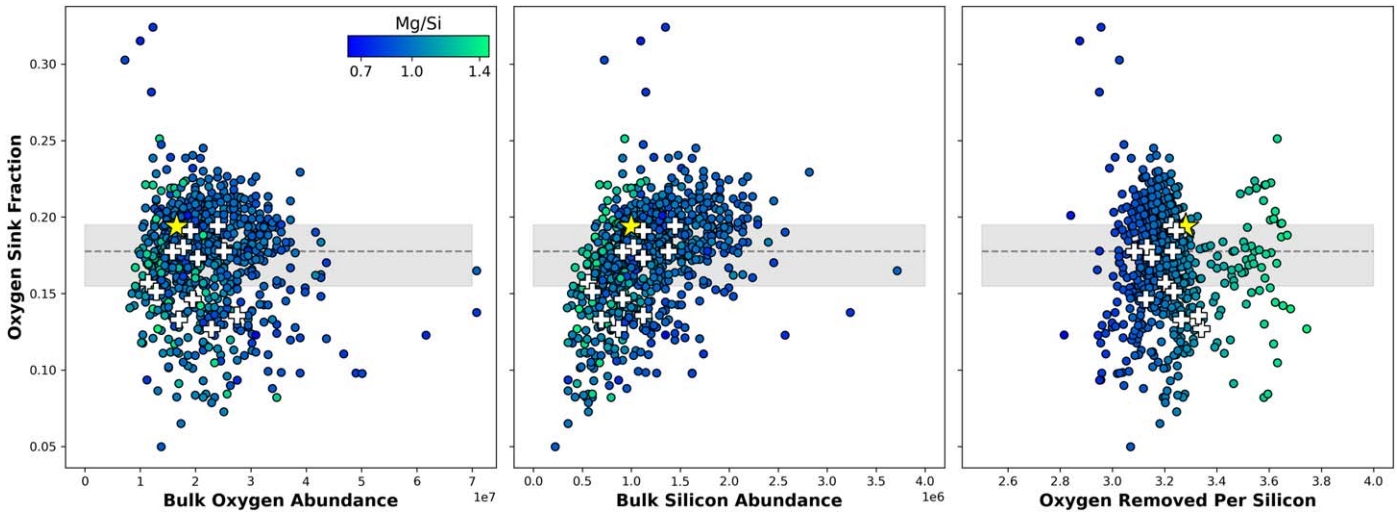

Figure 2. Oxygen sink fraction (O_{sink}) as function of bulk oxygen abundance (left), bulk silicon abundance (middle), and oxygen removed per silicon (right). Circles represent the solar neighborhood sample from Brewer et al. (2016) colored by their Mg/Si ratio. White crosses indicate the subset of compositional benchmarks, and the yellow star represents the Sun. The gray dashed line shows the median oxygen sink fraction for the total solar neighborhood population, with the shaded region bounding the first and third quartiles.

$$\Sigma\mathrm{Si} = \mathrm{A}_{\mathrm{Mg_2SiO_4}} + \mathrm{A}_{\mathrm{MgSiO_3}} \tag{14}$$

$$A_{\mathrm{Mg_2SiO_4}} = \Sigma\mathrm{Mg} - \Sigma\mathrm{Si}, \tag{15}$$

where A_X is the abundance of a given condensate species and ΣN is the abundance of a given element.

From this example, we can see that, in a gas where Mg/Si $>$ 1, forsterite effectively serves as a sink for "excess" magnesium. If Mg/Si $=$ 1, no forsterite condenses and the only oxygen-rich condensate is enstatite. If Mg/Si $<$ 1, the above expression gives a nonphysical result (i.e., a mass-balance violation) for forsterite. In this case, we have a system characterized by "excess" Si, which is able to condense into Mg-free species, namely quartz (SiO_2).

However, as previously stated, other Mg- and Si-bearing condensates exist and can impact the available inventories of magnesium and silicon. The most abundant of the minor refractory species are diopside ($CaMgSi_2O_6$) and anorthite ($CaAl_2Si_2O_8$) (Allard et al. 2001; Lodders 2002; Visscher et al. 2010a). We can take the first-order approximation example from above and extend it to include these refractory species by assuming that anorthite is the main Al-bearing condensate and diopside is the main Ca-bearing condensate (in the very rare case where $2\Sigma\mathrm{Al} > \Sigma\mathrm{Ca}$, anorthite becomes Ca-limited and the excess Al can form spinel, $MgAl_2O_4$). Assuming complete condensation of Ca and Al, the available inventories of Mg and Si at altitudes where we might consider forsterite, enstatite, or quartz as possible condensates are given by

$$N_{\mathrm{Mg}} \approx \Sigma\mathrm{Mg} - A_{\mathrm{CaMgSi_2O_6}} \tag{16}$$

$$N_{\mathrm{Si}} \approx \Sigma\mathrm{Si} - 2A_{\mathrm{CaMgSi_2O_6}} - 2A_{\mathrm{CaAl_2Si_2O_8}}. \tag{17}$$

The forsterite regime threshold (see Equation (15)) is then

$$A_{\mathrm{Mg_2SiO_4}} \approx \Sigma\mathrm{Mg} + \Sigma\mathrm{Ca} + 0.5\Sigma\mathrm{Al} - \Sigma\mathrm{Si}, \tag{18}$$

where a nonphysical value ($A_{\mathrm{Mg_2SiO_4}} < 0$) again indicates an excess of Si and the formation of SiO_2. Using element abundances from the Brewer et al. (2016) solar neighborhood sample, this second-order stoichiometric approximation suggests a condensation regime highly sensitive to the bulk atmospheric Mg/Si ratio (ΣMg/ΣSi). For ΣMg/ΣSi $\gtrsim$0.9, we anticipate the condensation of enstatite + forsterite, whereas for ΣMg/ΣSi $\lesssim$0.9, we anticipate enstatite + quartz.

In the following section, we discuss variations in the predicted silicate condensation sequence over a range of observed solar neighborhood stellar abundances via Brewer et al. (2016) and as a function of the Mg/Si ratio.

7. Sequestered Oxygen in Compositional Benchmark Brown Dwarfs

In the following subsections, we summarize the results of using stellar elemental abundances in compositional benchmark systems to predict the oxygen sink fraction and the silicate cloud regime. Additionally, we calculate these values for the Brewer et al. (2016) solar neighborhood sample, to give a population overview of what we might expect to see for the entire compositional benchmark sample (see Section 1) as well as brown dwarfs in the local region.

7.1. Effective Oxygen Removal in Ultracool Dwarf Atmospheres

Using the mass-balance and stoichiometric calculations explained above, we calculate an oxygen sink fraction, or the fraction of bulk oxygen lost to condensates in a UCD atmosphere, for the solar neighborhood as shown in Figure 2. We highlight the individual compositional benchmark systems among this larger sample to illustrate the potential for large variations in chemistry to exist. However, we plot the median of this entire sample such that the chemical distribution of the local solar neighborhood lends itself to an oxygen sink of approximately $17.8^{+1.7}_{-2.3}$% (or $O_{sink} \approx 0.178^{+0.017}_{-0.023}$). This is an upper limit estimate made while assuming, not unreasonably, that all Mg-, Si-, Ca-, Al-, Ti-, and V-bearing oxides condense out at various points in the UCD atmosphere.

In Figure 2, we show how this oxygen sink varies with bulk oxygen abundance such that, in relatively oxygen-rich atmospheres, the refractory elements have a lesser fractional impact, while the opposite is true for relatively oxygen-poor environments. In relatively oxygen-poor stars, we find that the bulk

abundances of Mg and Si are not necessarily uniformly depleted relative to oxygen, thereby sequestering a larger fraction of oxygen in clouds. Additionally, we illustrate that the oxygen sink fraction trends intuitively with bulk silicon abundance such that systems with more silicon will sequester oxygen into clouds at a larger fractional occurrence. Finally, we show the variance in "oxygen removed per silicon atom"—a parameter defined in Burrows & Sharp (1999) to describe the amount of oxygen in condensates. Burrows & Sharp (1999) estimated an O/Si removal factor of ∼3.28 using solar abundances from Anders & Grevesse (1989), while here we illustrate the scatter introduced by using elemental abundances from a larger stellar sample. We find a median O/Si removal factor of $\sim 3.19^{+0.05}_{-0.06}$, which intuitively trends with Mg/Si such that systems with higher Mg/Si ratios will have higher O/Si ratios (see Equation (9)). However, we show that O/Si does not trend with the oxygen sink fraction and is therefore not a useful metric, on its own, to estimate the total oxygen removed due to clouds.

The predicted median oxygen sink fraction here is ∼10 percentage points less than that estimated in previous retrieval modeling work on T-type dwarfs (e.g., Line et al. 2015; Calamari et al. 2022), potentially driving the high brown dwarf C/O ratio trend discussed in Calamari et al. (2022) even steeper. If only ∼18% of total oxygen is being lost to clouds, we have to consider what other types of dynamical processes could be occurring in these atmospheres.

Additionally, we show a predictive relation between the above- and below-cloud, or observed and bulk, C/O ratio in Figure 3 as laid out in Section 6.1 via Equation (12). We determine a fit to this data based on the behavior of Mg/O, Si/O, and Mg/Si ratios as bulk C/O increases. This generally correlates with a median oxygen sink fraction of ∼18% for the solar neighborhood population. However, we do show how observed C/O ratio increases nonlinearly as bulk C/O increases—a function of the fact that element abundances of O, Mg, and Si in metal-poor systems are not necessarily uniformly depleted. As such, as bulk C/O ratio increases, or bulk oxygen abundance decreases (see Figure 2), there is a nonlinear increase in oxygen sink fraction, which effects the observed UCD C/O ratio. This fit provides some guidelines for what we might expect, given UCD retrieval model outputs.

7.2. Predicted Silicate Cloud Regime

While the range in stellar elemental abundances creates variance in the oxygen sink fraction, it minimally impacts the silicate regime threshold, which is highly sensitive to the Mg/Si ratio. This behavior is demonstrated in Figure 4, which shows the equilibrium distribution of O-bearing phases at 1000 K and 1 bar as a function of ΣMg/ΣSi in an otherwise solar-composition gas (solar Mg/Si = 1.03 using abundances from Lodders 2021). This $P-T$ point was chosen because it is generally representative of UCD photospheric temperatures and pressures, and it also lies above Mg-silicate cloud condensation $P-T$ points, thus capturing the upper limit of oxygen sequestration.

Figure 4 shows a Mg/Si ratio threshold value of ∼0.9, such that UCD companions may be expected to exhibit the following equilibrium silicate condensate regime:

1. Mg/Si $\lesssim$0.9 : Enstatite + Quartz
2. Mg/Si ∼0.9 : Enstatite
3. Mg/Si $\gtrsim$0.9 : Enstatite + Forsterite,

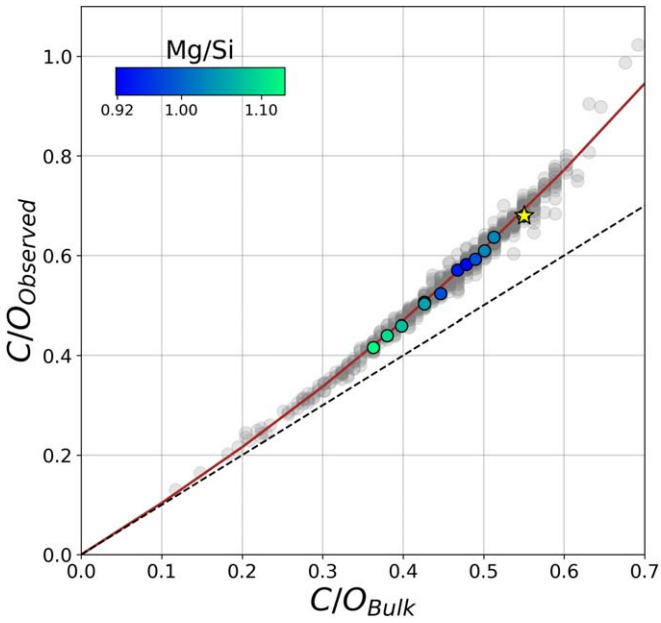

Figure 3. The predicted observed C/O ratio in a UCD companion as a function of the system's bulk C/O ratio, using stellar elemental abundances from Brewer et al. (2016) and assuming removal of oxygen via condensation of metal oxides. The dashed line indicates the 1:1 line. The red curve is the estimated $(C/O)_{obs}$ from Equation (12). The star indicates $(C/O)_{bulk}$ and the predicted $(C/O)_{obs}$ ratio using solar elemental abundances from Lodders (2021). Circles represent the compositional benchmarks subset colored by Mg/Si ratio, while gray points show the solar neighborhood sample from Brewer et al. (2016).

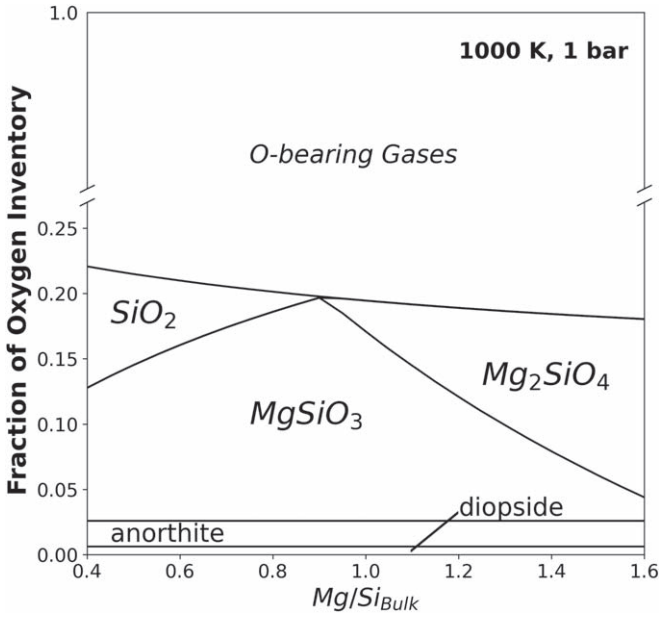

Figure 4. Predicted silicate regime and distribution of oxygen into condensates and vapor at 1000 K and 1 bar, based upon thermochemical equilibrium calculations over a range of bulk Mg/Si element abundance ratios in an otherwise solar-composition atmosphere. The fraction of the oxygen inventory removed into condensates corresponds to O_{sink} as described in the text.

consistent with the second-order approximation described above (see Equation (18)). Moreover, we find that Mg-silicate condensation behavior is relatively independent of varying Ca and Al abundances, etc., suggesting that this threshold may serve as a guide to differentiating silicate cloud regimes in UCD atmospheres. For example, this finding is in agreement

with previous retrieval work in Burningham et al. (2021), where the best-fit model for the L4.5 dwarf, 2MASSW J2224438-015852, was a layered cloud model consisting of enstatite, quartz, and iron with an inferred $Mg/Si = 0.69$.

It is important to keep in mind that the particular sequence and identity of cloud condensate phases in a given UCD atmosphere will be subject to each object's atmospheric properties including element abundance patterns, thermal structure, mixing, condensate re-equilibration, and gravity. Indeed, several works have suggested, by closely examining both low- and medium-resolution optical and near-infrared spectra as well as the scatter on color–magnitude diagrams, that there is an atmospheric difference in young L dwarfs versus field L dwarfs. This difference can be linked to a low surface gravity in the former; see, e.g., Faherty et al. (2012, 2016) and Suárez & Metchev (2023). However, given these possible variations, the stoichiometric approach presented here provides a robust estimate of oxygen removal into refractory condensates and an estimate of atmospheric C/O inventories over a broad range of UCD atmospheres.

8. Future Applications in Extrasolar World Modeling

In order to utilize these theoretical predictions, we turn back to retrieval modeling for brown dwarfs, as this is currently the only modeling technique that can explore the unique chemistry and thermodynamics of individualized spectra. These thermochemical predictions will act as guidelines but not constraints in future modeling attempts for compositional benchmarks. In particular, having empirical knowledge about the system will help ground our results in what is already known rather than act as an a priori constraint, potentially biasing results.

In future work, we will specifically return to the compositional benchmark sample outlined in Table 2 and shown in Figures 2 and 3. Of the 12 systems with well-characterized host stars, 10 have L-dwarf companions that would be excellent candidates for detailed cloud modeling via retrievals. However, only four systems (HD 130948BC, HD 203030B, HR 7672B, and HD 4747B) have available near-infrared (NIR) spectral data. Additionally, only two of these four systems have full NIR spectral coverage (1–2.5 μm), which has been shown to be the minimum necessary requirement for robust retrieval modeling (Burningham et al. 2021). Beyond NIR spectral coverage alone, Burningham et al. (2021), Calamari et al. (2022), and Vos et al. (2023) demonstrated the need for mid-infrared (MIR) spectral coverage in order to fully model molecular abundances and characterize condensate cloud species. In order to capitalize on the entire compositional benchmark sample outlined in Table 1, we will continue to require and employ the use of telescopes such as the James Webb Space Telescope (JWST) to provide detailed and full spectral coverage (1–28 μm) of these objects. Additionally, we will rely on optical telescopes such as HIRES on Keck or PEPSI on the Large Binocular Telescope (LBT) to obtain spectral coverage on the primaries listed in Table 1 to continue characterization of these systems.

By obtaining full spectral coverage for L-type objects in the compositional benchmarks sample, we can then begin to conduct a suite of models (both cloudy and cloudless) where we might expect a best-fit cloud model for each object in this sample to fall into the $Mg/Si > 0.9$ (enstatite + forsterite) cloud regime. A result counter to that expected would certainly be cause for discussion on the chemical makeup of the UCD companion and its origins.

Additionally, we can apply the oxygen sink correction in future work in the way that has been done in Line et al. (2015, 2017), Zalesky et al. (2022), and Calamari et al. (2022)—increasing retrieved oxygen abundance by the percentage lost to clouds. However, this will be a much closer approximation to a true oxygen sink in these atmospheres, because we have accounted for system-specific elemental abundances. While our median oxygen sink fraction is a good estimation for oxygen lost to clouds in UCDs that are solitary or have unknown host star chemistry, the compositional benchmark sample outlined in Table 2 has fractions uniquely specific to each system. This subset of host star chemistry reveals variances in the oxygen sink fraction from 13% to 19%. Again, we might expect to see trends toward high C/O ratios (or relatively low retrieved oxygen abundances) strengthen as a result of this work. The population of brown dwarfs with a $C/O > 0.8$ will likely increase. As a result, oxygen loss in brown dwarf atmospheres remains an open question to be explored.

Finally, the work presented here has implications for the atmospheric modeling of gas giant exoplanets whose effective temperatures ($T_{\rm eff}$) cross into the L- and T-dwarf regime. While exoplanet modeling cannot assume co-evality as we do here, given the uncertainty in and influence of the formation process on those worlds, sequestration of oxygen into refractory condensates will certainly impact retrieved molecular abundances in those temperature atmospheres. Despite the added complications of processes such as late-stage accretion, planetary migration, and atmospheric differentiation, host star abundance analysis is essential in order to reconstruct formation history. Moreover, the approach described here can provide clues to oxygen sequestration into condensate phases and estimates of bulk composition based on observed abundances of C- and O-bearing species in exoplanet atmospheres.

9. Conclusions

In this work, we present evidence in favor of using brown dwarfs in co-moving systems with F, G, or K-type stars ("compositional benchmarks") to ground our exploration and understanding of the thermodynamic and chemical processes in brown dwarfs. As F, G, and K-type stars often have a wealth of data available, this provides us with external empirical information that will help ground our modeling in our attempt to disentangle what the fundamental properties of brown dwarfs, such as the C/O ratio, are telling us about their atmospheres and formation histories.

Specifically, we have used published elemental abundances for a sample of compositional benchmarks, along with the local solar neighborhood population, from Brewer et al. (2016) to provide us with two empirical constraints: oxygen sink fraction and predicted silicate regime. Through a series of stoichiometric and mass-balance calculations, we have determined that, given the bulk elemental abundances from a primary host star, the median oxygen sink in the companion UCD atmosphere is $17.8^{+1.7}_{-2.3}$%. This update provides context for previous work (e.g., Burrows & Sharp 1999; Lodders & Fegley 2002; Visscher & Fegley 2005; Visscher & Moses 2011; Line et al. 2015) that have based oxygen sink estimates upon solar elemental abundances. We have also used the elemental abundances of our primary stars to determine the Mg/Si ratio

threshold at which the silicate cloud composition transitions from enstatite ($MgSiO_3$) + quartz (SiO_2) clouds (Mg/Si < 0.9) to enstatite + forsterite (Mg_2SiO_4) clouds (Mg/Si > 0.9).

Our global aim in this work is to utilize these chemical predictions in future brown dwarf retrieval modeling studies to help understand the thermochemical dynamics of cloud processes and oxygen sequestration in these atmospheres. By carefully studying brown dwarf atmospheric chemistry, we are one step closer to uncovering the formation and evolution pathways of these objects.

Acknowledgments

This work was supported by the National Science Foundation via awards AST-1909776 and AST-1909837 and NASA via award 80NSSC22K0142. This work also benefited from the 2022 Exoplanet Summer Program in the Other Worlds Laboratory (OWL) at the University of California, Santa Cruz, a program funded by the Heising-Simons Foundation. B. Burningham acknowledges support from UK Research and Innovation Science and Technology Facilities Council [ST/X001091/1]. C. Visscher acknowledges support from JWST Cycle 1 AR 2232. The authors thank John M. Brewer for helpful discussions and comments that improved this work.

ORCID iDs

Emily Calamari https://orcid.org/0000-0002-2682-0790
Jacqueline K. Faherty https://orcid.org/0000-0001-6251-0573
Channon Visscher https://orcid.org/0000-0001-6627-6067
Marina E. Gemma https://orcid.org/0000-0002-8871-773X
Ben Burningham https://orcid.org/0000-0003-4600-5627
Austin Rothermich https://orcid.org/0000-0003-4083-9962

References

Ackerman, A. S., & Marley, M. S. 2001, ApJ, 556, 872
Adibekyan, V. Z., Sousa, S. G., Santos, N. C., et al. 2012, A&A, 545, A32
Allard, F., Guillot, T., Ludwig, H. G., et al. 2003, in IAU Symp. 211, Brown Dwarfs, ed. E. Martín (San Francisco, CA: ASP), 325
Allard, F., Hauschildt, P. H., Alexander, D. R., & Starrfield, S. 1997, ARA&A, 35, 137
Allard, F., Hauschildt, P. H., Alexander, D. R., Tamanai, A., & Schweitzer, A. 2001, ApJ, 556, 357
Anders, E., & Grevesse, N. 1989, GeCoA, 53, 197
Bihain, G., Rebolo, R., Zapatero Osorio, M. R., Béjar, V. J. S., & Caballero, J. A. 2010, A&A, 519, A93
Bowler, B. P., Liu, M. C., & Cushing, M. C. 2009, ApJ, 706, 1114
Bowler, B. P., Shkolnik, E. L., Liu, M. C., et al. 2015, ApJ, 806, 62
Brewer, J. M., & Fischer, D. A. 2016, ApJ, 831, 20
Brewer, J. M., Fischer, D. A., Basu, S., Valenti, J. A., & Piskunov, N. 2015, ApJ, 805, 126
Brewer, J. M., Fischer, D. A., Valenti, J. A., & Piskunov, N. 2016, ApJS, 225, 32
Burgasser, A. J., Geballe, T. R., Leggett, S. K., Kirkpatrick, J. D., & Golimowski, D. A. 2006, ApJ, 637, 1067
Burgasser, A. J., Kirkpatrick, J. D., Brown, M. E., et al. 2002, ApJ, 564, 421
Burgasser, A. J., Kirkpatrick, J. D., Cutri, R. M., et al. 2000, ApJL, 531, L57
Burgasser, A. J., Kirkpatrick, J. D., & Lowrance, P. J. 2005a, AJ, 129, 2849
Burgasser, A. J., Reid, I. N., Leggett, S. K., et al. 2005b, ApJL, 634, L177
Burningham, B., Cardoso, C. V., Smith, L., et al. 2013, MNRAS, 433, 457
Burningham, B., Faherty, J., Gagné, J., Mann, A., & Hung, C. L. 2018, RNAAS, 2, 207
Burningham, B., Faherty, J. K., Gonzales, E. C., et al. 2021, MNRAS, 506, 1944
Burningham, B., Marley, M. S., Line, M. R., et al. 2017, MNRAS, 470, 1177
Burningham, B., Pinfield, D. J., Leggett, S. K., et al. 2009, MNRAS, 395, 1237
Burrows, A., Marley, M., Hubbard, W. B., et al. 1997, ApJ, 491, 856
Burrows, A., & Sharp, C. M. 1999, ApJ, 512, 843
Burrows, A., Sudarsky, D., & Lunine, J. I. 2003, ApJ, 596, 587
Calamari, E., Faherty, J. K., Burningham, B., et al. 2022, ApJ, 940, 164
Canty, J. I., Lucas, P. W., Yurchenko, S. N., et al. 2015, MNRAS, 450, 454
Carlson, B. E., Prather, M. J., & Rossow, W. B. 1987, ApJ, 322, 559
Casey, A. R., Hogg, D. W., Ness, M., et al. 2016, arXiv:1603.03040
Chabrier, G., Baraffe, I., Allard, F., & Hauschildt, P. 2000, ApJ, 542, 464
Chambers, K. C., Magnier, E. A., Metcalfe, N., et al. 2016, arXiv:1612.05560
Chauvin, G., Lagrange, A. M., Zuckerman, B., et al. 2005, A&A, 438, L29
Cheetham, A., Ségransan, D., Peretti, S., et al. 2018, A&A, 614, A16
Chiu, K., Fan, X., Leggett, S. K., et al. 2006, AJ, 131, 2722
Crepp, J. R., Gonzales, E. J., Bechter, E. B., et al. 2016, ApJ, 831, 136
Crepp, J. R., Johnson, J. A., Fischer, D. A., et al. 2012, ApJ, 751, 97
Currie, T., Brandt, T. D., Kuzuhara, M., et al. 2020, ApJL, 904, L25
Cushing, M. C., Roellig, T. L., Marley, M. S., et al. 2006, ApJ, 648, 614
Deacon, N. R., Liu, M. C., Magnier, E. A., et al. 2014, ApJ, 792, 119
Delgado Mena, E., Adibekyan, V., Santos, N. C., et al. 2021, A&A, 655, A99
Dupuy, T. J., Liu, M. C., & Ireland, M. J. 2009, ApJ, 692, 729
Dupuy, T. J., Liu, M. C., & Ireland, M. J. 2014, ApJ, 790, 133
Faherty, J. K., Beletsky, Y., Burgasser, A. J., et al. 2014, ApJ, 790, 90
Faherty, J. K., Burgasser, A. J., Walter, F. M., et al. 2012, ApJ, 752, 56
Faherty, J. K., Burgasser, A. J., West, A. A., et al. 2010, AJ, 139, 176
Faherty, J. K., Gagné, J., Popinchalk, M., et al. 2021, ApJ, 923, 48
Faherty, J. K., Riedel, A. R., Cruz, K. L., et al. 2016, ApJS, 225, 10
Fegley, B. J, & Lodders, K. 1996, ApJL, 472, L37
Gagné, J., Faherty, J. K., Cruz, K. L., et al. 2015, ApJS, 219, 33
Gaia Collaboration, Klioner, S. A., Mignard, F., et al. 2021, A&A, 649, A9
Geballe, T. R., Knapp, G. R., Leggett, S. K., et al. 2002, ApJ, 564, 466
Gomes, J. I., Pinfield, D. J., Marocco, F., et al. 2013, MNRAS, 431, 2745
Gonzales, E. C., Burningham, B., Faherty, J. K., et al. 2020, ApJ, 905, 46
Grant, D., Lewis, N. K., Wakeford, H. R., et al. 2023, ApJL, 956, L29
Hawkins, K. 2023, MNRAS, 525, 3318
Helling, C., & Casewell, S. 2014, A&ARv, 22, 80
King, R. R., McCaughrean, M. J., Homeier, D., et al. 2010, A&A, 510, A99
Kirkpatrick, J. D. 2005, ARA&A, 43, 195
Kirkpatrick, J. D., Dahn, C. C., Monet, D. G., et al. 2001, AJ, 121, 3235
Kirkpatrick, J. D., Reid, I. N., Liebert, J., et al. 2000, AJ, 120, 447
Kitzmann, D., Heng, K., Oreshenko, M., et al. 2020, ApJ, 890, 174
Kuchner, M. J., Faherty, J. K., Schneider, A. C., et al. 2017, ApJL, 841, L19
Kuzuhara, M., Currie, T., Takarada, T., et al. 2022, ApJL, 934, L18
Lewis, J. S. 1969, Icar, 10, 365
Line, M. R., Marley, M. S., Liu, M. C., et al. 2017, ApJ, 848, 83
Line, M. R., Teske, J., Burningham, B., Fortney, J. J., & Marley, M. S. 2015, ApJ, 807, 183
Liu, M. C., Dupuy, T. J., & Leggett, S. K. 2010, ApJ, 722, 311
Liu, M. C., Fischer, D. A., Graham, J. R., et al. 2002, ApJ, 571, 519
Lodders, K. 1999, ApJ, 519, 793
Lodders, K. 2002, ApJ, 577, 974
Lodders, K. 2003, ApJ, 591, 1220
Lodders, K. 2004, Sci, 303, 323
Lodders, K. 2010, in Formation and Evolution of Exoplanets, ed. R. Barnes (New York: Wiley), 157
Lodders, K. 2021, SSRv, 217, 44
Lodders, K., & Fegley, B. 2002, Icar, 155, 393
Lodders, K., & Fegley, B. 2006, in Astrophysics Update 2, ed. J. W. Mason (Chichester: Praxis Publishing Ltd), 1
Lodieu, N., Pérez-Garrido, A., Béjar, V. J. S., et al. 2014, A&A, 569, A120
Luhman, K. L., Patten, B. M., Marengo, M., et al. 2007, ApJ, 654, 570
Lunine, J. I., Hubbard, W. B., & Marley, M. S. 1986, ApJ, 310, 238
Madhusudhan, N. 2012, ApJ, 758, 36
Maire, A. L., Baudino, J. L., Desidera, S., et al. 2020, A&A, 633, L2
Mann, A. W., Brewer, J. M., Gaidos, E., Lépine, S., & Hilton, E. J. 2013, AJ, 145, 52
Marley, M. S., Saumon, D., Guillot, T., et al. 1996, Sci, 272, 1919
Marley, M. S., Ackerman, A. S., Cuzzi, J. N., & Kitzmann, D. 2013, in Comparative Climatology of Terrestrial Planets, ed. S. J. Mackwell et al. (Tucson, AZ: University of Arizona Press), 367
Marley, M. S., Gelino, C., Stephens, D., Lunine, J. I., & Freedman, R. 1999, ApJ, 513, 879
Marley, M. S., Seager, S., Saumon, D., et al. 2002, ApJ, 568, 335
Marocco, F., Pinfield, D. J., Cook, N. J., et al. 2017, MNRAS, 470, 4885
Marocco, F., Smart, R. L., Mamajek, E. E., et al. 2020, MNRAS, 494, 4891
Metchev, S. A., & Hillenbrand, L. A. 2004, ApJ, 617, 1330
Miles, B. E., Skemer, A. J. I., Morley, C. V., et al. 2020, AJ, 160, 63
Mollière, P., Stolker, T., Lacour, S., et al. 2020, A&A, 640, A131
Morley, C. V., Fortney, J. J., Marley, M. S., et al. 2012, ApJ, 756, 172
Mugrauer, M., Seifahrt, A., Neuhäuser, R., & Mazeh, T. 2006, MNRAS, 373, L31
Nakajima, T., Oppenheimer, B. R., Kulkarni, S. R., et al. 1995, Natur, 378, 463

Ness, M., Hogg, D. W., Rix, H. W., Ho, A. Y. Q., & Zasowski, G. 2015, ApJ, 808, 16
Noll, K. S., Geballe, T. R., & Marley, M. S. 1997, ApJL, 489, L87
Öberg, K. I., Murray-Clay, R., & Bergin, E. A. 2011, ApJL, 743, L16
Oppenheimer, B. R., Kulkarni, S. R., Matthews, K., & Nakajima, T. 1995, Sci, 270, 1478
Oppenheimer, B. R., Kulkarni, S. R., Matthews, K., & van Kerkwijk, M. H. 1998, ApJ, 502, 932
Pinfield, D. J., Burningham, B., Lodieu, N., et al. 2012, MNRAS, 422, 1922
Pinfield, D. J., Jones, H. R. A., Lucas, P. W., et al. 2006, MNRAS, 368, 1281
Potter, D., Martín, E. L., Cushing, M. C., et al. 2002, ApJL, 567, L133
Prinn, R. G., & Barshay, S. S. 1977, Sci, 198, 1031
Rebolo, R., Zapatero Osorio, M. R., & Martín, E. L. 1995, Natur, 377, 129
Reid, I. N., Lewitus, E., Allen, P. R., Cruz, K. L., & Burgasser, A. J. 2006, AJ, 132, 891
Rice, M., & Brewer, J. M. 2020, ApJ, 898, 119
Rickman, E. L., Ségransan, D., Hagelberg, J., et al. 2020, A&A, 635, A203
Rothermich, A., Faherty, J. K., Bardalez-Gagliuffi, D., et al. 2023, AAS Meeting, 241, 203.12
Schneider, A. C., Meisner, A. M., Gagné, J., et al. 2021, ApJ, 921, 140
Seifahrt, A., Reiners, A., Almaghrbi, K. A. M., & Basri, G. 2010, A&A, 512, A37
Skrutskie, M. F., Cutri, R. M., Stiening, R., et al. 2006, AJ, 131, 1163
Skrzypek, N., Warren, S. J., & Faherty, J. K. 2016, A&A, 589, A49
Suárez, G., & Metchev, S. 2022, MNRAS, 513, 5701
Suárez, G., & Metchev, S. 2023, MNRAS, 523, 4739
Teske, J. K., Thorngren, D., Fortney, J. J., Hinkel, N., & Brewer, J. M. 2019, AJ, 158, 239
Tsuji, T. 1964, PJAB, 40, 99
Tsuji, T., & Nakajima, T. 2014, PASJ, 66, 98
Tsuji, T., Nakajima, T., & Takeda, Y. 2015, PASJ, 67, 26
Tsuji, T., Ohnaka, K., Aoki, W., & Nakajima, T. 1996, A&A, 308, L29
Twarog, B. A. 1980, ApJ, 242, 242
Visscher, C., & Fegley, B. J. 2005, ApJ, 623, 1221
Visscher, C., Lodders, K., & Fegley, B. J 2006, ApJ, 648, 1181
Visscher, C., Lodders, K., & Fegley, B. J 2010a, ApJ, 716, 1060
Visscher, C., & Moses, J. I. 2011, ApJ, 738, 72
Visscher, C., Moses, J. I., & Saslow, S. A. 2010b, Icar, 209, 602
Vos, J. M., Burningham, B., Faherty, J. K., et al. 2023, ApJ, 944, 138
Wakeford, H. R., Visscher, C., Lewis, N. K., et al. 2017, MNRAS, 464, 4247
Wang, J., Kolecki, J. R., Ruffio, J. B., et al. 2022, AJ, 163, 189
Wilson, J. C., Kirkpatrick, J. D., Gizis, J. E., et al. 2001, AJ, 122, 1989
Wright, E. L., Eisenhardt, P. R. M., Mainzer, A. K., et al. 2010, AJ, 140, 1868
Zalesky, J. A., Line, M. R., & Schneider, A. C. 2019, ApJ, 877, 24
Zalesky, J. A., Saboi, K., Line, M. R., et al. 2022, ApJ, 936, 19
Zhang, Z. H., Pinfield, D. J., Day-Jones, A. C., et al. 2010, MNRAS, 404, 1817